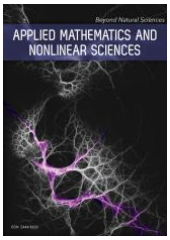

Applied Mathematics and Nonlinear Sciences

https://www.sciendo.com

Dynamics Response of Rail Vehicle Induced by Incorporating Electric-Dominated Transmission Component

Changxiu Yang†

1. Department of Rail Transit, Chongqing Vocational College of Transportation, Chongqing, China

Submission Info

Communicated by Z. Sabir
Received October 12, 2023
Accepted January 15, 2024
Available online February 15, 2024

Abstract

As an important component of train speed regulation, traction transmission system is the power source and the main transmission component of traction force. Its dynamic characteristics can affect the dynamic performance of vehicle system to a certain extent. With the rapid development of rail train transportation in China, the running speed of the train continues to improve, the dynamic characteristics of the vehicle is becoming more complex, and the influence of the electrical part of the traction transmission system gradually appears. The motor and gearbox are crucial components of the train power bogie to complete the conversion and transmission of electric energy to mechanical energy, with their dynamic characteristics are most directly affected by the electrical characteristics of the traction system. In this work, a vehicle electro-mechanical coupling mathematical model based on multi-body dynamics was established by explicitly incorporating the electric-induced traction into the transmission system, to study the influence of traction system vibration on vehicle dynamics. The dynamics responses of the lateral and longitudinal vibration on vehicle motor and gearbox were quantitatively analysed from the traction drive system. Compared with the line test, it was observed that 12-times of the fundamental frequency of the rotor has a great influence on the motor and gearbox.

Keywords: Traction drive system; Electro-mechanical coupling; Dynamic characteristics
AMS 2020 codes: 93B15

†Corresponding author.
Email address: cvct_cqjy@163.com

ISSN 2444-8656
https://doi.org/10.2478/amns-2024-0011

1 Introduction

Rail vehicle transportation has been attracting intensive attention in the world especially in China, showing the unique technical and economic advantages. Transmission system is the key subsystem of rail transit vehicles, which is responsible for providing power for the operation of the whole train. The traction drive system of rail vehicle adopted sinusoidal pulse width modulation (SPWM) technology to invert DC into three-phase AC with adjustable voltage and frequency, which could be supplied to traction asynchronous motor. During operation [1], the electromagnetic torque outputs by traction motor would act on the pinion shaft through the elastic coupling. The big gear and the axle were in interference fit, and then could drive the wheel-set [2][3][4]. Through the motor control unit, the smooth speed regulation of the motor could be realized, and then the speed regulation of the rail vehicle could be achieved. For Metro train, DC power [5] from catenary was directly applied through pantograph, while for high-speed rail vehicles, a step-down rectification process, i.e., from AC to DC power, should be incorporated prior to traction inverter system.

Schematic diagram of a typical electrification structure for metro [6] traction drive system is shown in Fig. 1a. Under the condition of metro train traction [7], DC power obtained from the catenary [8] was output to the traction inverter through the intermediate DC link [9]. The traction inverter would convert the DC power into AC power [10] and output it to the traction asynchronous motor. At the braking condition, three-phase AC outputs from traction motor could be converted into DC by traction inverter [11], and transferred it to the catenary through the intermediate DC link. However, for high-speed railway, two more additional modules exist in the condition of traction [12] and braking, i.e., transformer and converter.

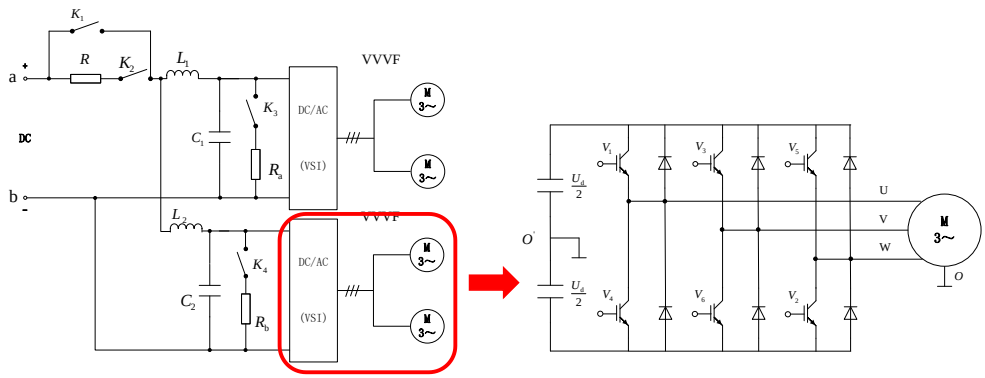

(a) Schematic diagram of Metro electric traction drive system

(b) Schematic diagram of SPWM inverter circuit

Figure 1. Schematic diagram of electrification for metro traction drive system.

Traction motor for rail transit [13] could output two variables, torque and speed, which determined the traction force and running speed of the train, respectively. And they could be regulated by three-phase AC with adjustable frequency and amplitude. In traction inverter [14], SPWM technology [15], adopting to achieve the three-phase AC, was to use a series of rectangular pulses with equal amplitude and different width to replace sine wave. The core of SPWM inverter was to control the on-off of IGBT in traction inverter to get SPWM waveform, as shown in Fig. 1b. Direct torque control method was adopted in traction inverter, that is, the space voltage vector was directly used to calculate and control the torque and flux of the motor in the stator coordinate system. In order to obtain the high dynamic performance [16] of torque, the stator field orientation was adopted and the space vector SPWM was generated by means of discrete two-point regulation to directly control the switching state of the inverter.

Field measurements on the vibrating characteristics of the car body (CB) and its suspended equipment (CBSE) were studied by Wu *et al.* [17] for a high-speed railway vehicle. In their long-term tracking test, the running stability of vehicle and wheel-rail interaction were also examined with the increase of operation distance (OD), i.e., a total of 2,400,000 km. Based on the theory of structural dynamics [18] and the principle of modal superposition method, the formula for calculating the dynamic stress of vibration fatigue was deduced by Wu *et al.* [19] [20] under non-stationary state.

The dynamics of the under-frame suspended equipment, such as gear-box, traction motor, on the vibrations of car-body had become a significant concern for rail vehicles. It was advised from the field tests that the dynamic unbalance [21] had a major influence on car-body vibrations, especially the local flexible vibration, which leaded to a decrease in the passenger ride comfort and may even cause structural damage to the car-body. Coupling model and vibration simulations of railway vehicles and running gear bearings were investigated by Wang *et al*. [22], a complete method for bearing modelling with multi-type defects was proposed. The bearing kinematics with three translation and one rotation degrees of freedom were analyzed and modeled, and defect modeling algorithms for the inner raceway, outer raceway and rollers were proposed [22]. Xu *et al*. [23] analyzed the self-excited torsional vibration of high-speed train drive system, their results showed that the vibration forms of the system were mainly determined by the relationships between the average creep rate [24] and the critical creep rate of the wheel driven directly by motors. Dao *et al*. [25] proposed a numerical method for the calculation of the frequencies of vibration of a car body on a high-speed electric multiple unit train with under-chassis-suspended equipment. These reports mainly focused on the vibrational behaviour [26] [27] and characteristic of the car-body or its corresponding component, however, the study of the influence induced from the traction drive especially the factor regarding the electric power was insufficient.

From a purely mechanical point of view, the traction transmission system of rail transit mainly include traction motor, gearbox, gear system [22], wheel-set [28] [29] and other related structural components, which exist in the power bogie [30] [31]. From a purely electrical view, it mainly included some electrical devices such as catenary system, pantograph catenary, motor control, and so on. Several parts consisting of power bogie within rail transit mainly are: wheel-set [32] [33], axle box, frame, primary suspension device, secondary suspension device, traction transmission device and basic braking device. Vehicle system was a complex mechanical system with multiple degrees of freedom, and its dynamic performance [34] [35] [36] was usually studied by the analysis method of multi-body system dynamics. In this work, an electro-mechanical coupling dynamic mathematical vehicle model was established based on vehicle system dynamics to study the influence of electric part of traction transmission system on rail vehicle system.

2 Establishment of electro-mechanical coupling simulation model

2.1 Mathematical model of traction motor

For the theoretical model of traction motor, within the two phase arbitrary rotating coordinate system, i.e., *dq* coordinate system, the mathematical model of asynchronous traction motor could be expressed as the following matrix equation:

1) Flux linkage equation

$$\begin{bmatrix} \psi_{sd} \\ \psi_{sq} \\ \psi_{rd} \\ \psi_{rq} \end{bmatrix} = \begin{bmatrix} L_s & 0 & L_m & 0 \\ 0 & L_s & 0 & L_m \\ L_m & 0 & L_r & 0 \\ 0 & L_m & 0 & L_r \end{bmatrix} \begin{bmatrix} i_{sd} \\ i_{sq} \\ i_{rd} \\ i_{rq} \end{bmatrix} \tag{1}$$

2) Voltage equation

$$\begin{bmatrix} U_{sd} \\ U_{sq} \\ U_{rd} \\ U_{rq} \end{bmatrix} = \begin{bmatrix} R_s + L_s p & -\omega_{dqs} L_s & L_m p & -\omega_{dqs} L_m \\ \omega_{dqs} L_s & R_s + L_s p & \omega_{dqs} L_m & L_m p \\ L_m p & -\omega_{dqr} L_m & R_r + L_r p & -\omega_{dqr} L_r \\ \omega_{dqr} L_m & L_m p & \omega_{dqr} L_r & R_r + L_r p \end{bmatrix} \begin{bmatrix} i_{sd} \\ i_{sq} \\ i_{rd} \\ i_{rq} \end{bmatrix} \tag{2}$$

3) Torque equation

$$T_e = n_p L_m (i_{sq} i_{rd} - i_{sd} i_{rq}) = \frac{3}{2} n_p \frac{L_m}{\sigma L s L r} |\psi_s| |\psi_r| \sin\theta \tag{3}$$

4) Equation of motion

$$T_e = T_L + \frac{J}{n_p} \frac{d_{\omega_r}}{dt} \tag{4}$$

Where: ψ_{sd} —d axis component of stator flux linkage. ψ_{sq} —q axis component of stator flux linkage. ψ_{rd} —d axis component of rotor flux linkage. ψ_{rq} —q axis component of rotor flux linkage. ψ_s —Stator flux linkage in three phase shafting. ψ_r —Rotor flux linkage in three phase shafting. U_{sd} —d axis component of stator voltage. U_{sq} —q axis component of stator voltage. U_{rd} —d axis component of rotor voltage. U_{rq} —q axis component of rotor voltage. i_{sd} —d axis component of stator current. i_{sq} —q axis component of stator current. i_{rd} —d axis component of rotor current. i_{rq} —q axis component of rotor current. L_s —Stator self-inductance. L_r —Rotor self-inductance. L_m —Mutual inductance of two phase winding. p —Differential operator. R_s —Stator resistance. R_r —Rotor resistance. n_p —Polar logarithm. ω_{dqs} —Angular velocity of the *dq* coordinate system relative to the stator. ω_{dqr} —Angular velocity of the *dq* coordinate system relative to the rotor. J —Moment of inertia. ω_r —Angular velocity of motor rotor. σ —The leakage inductance of the motor. θ —The angle between the stator flux linkage and the rotor flux linkage.

Traction motor adopts SPWM inverter, which could be easy to realize and could effectively suppress low order harmonics, but it would lead to the increase of high order harmonics. When these harmonics [15] enter the traction motor [37], it would lead to harmonic torque, cause vibration, and then affect the dynamic performance [38] [39] of the vehicle. When the harmonic magnetic flux did not synchronize with the frequency of harmonic rotor current, their interaction would generate vibration harmonic torque. If the *n* rotating magnetic fields were generated by the fundamental and harmonic waves in the air gap, there would be (n^2-n) vibration harmonic torques by the interaction between the

fundamental wave rotating magnetic field and the harmonic rotor current. For example, the instantaneous value of the torque generated by the 5 stator harmonic current and the fundamental flux in each phase of the motor could be expressed as:

$$T_{\mathrm{A5-1}} = \frac{n_{\mathrm{p}}}{2\pi f_1}\sqrt{2}I_{25}\sin(5\omega t-\phi_2)\sqrt{2}E_2\sin\omega t \tag{5}$$

$$T_{\mathrm{B5-1}} = \frac{n_{\mathrm{p}}}{2\pi f_1}\sqrt{2}I_{25}\sin\left[(5\omega t-\phi_2)+\frac{2\pi}{3}\right]\sqrt{2}E_2\sin\left(\omega t-\frac{2\pi}{3}\right) \tag{6}$$

$$T_{\mathrm{C5-1}} = \frac{n_{\mathrm{p}}}{2\pi f_1}\sqrt{2}I_{25}\sin\left[(5\omega t-\phi_2)-\frac{2\pi}{3}\right]\sqrt{2}E_2\sin\left(\omega t-\frac{4\pi}{3}\right) \tag{7}$$

Where: E_2—The calculated value of the rotor electromotive force of the fundamental wave. ϕ_2—The phase difference between the current and the electromotive force at ωt=0, can be calculated according to the fundamental wave vector graph and the harmonic vector graph.

Trigonometric function relation type $\sin\alpha\sin\beta=\frac{1}{2}\left[\cos(\alpha-\beta)-\cos(\alpha+\beta)\right]$ was applied, these could be obtained as:

$$T_{\mathrm{A5-1}} = \frac{n_{\mathrm{p}}}{2\pi f_1}I_{25}E_2\left[\cos(4\omega t-\phi_2)-\cos(6\omega t-\phi_2)\right] \tag{8}$$

$$T_{\mathrm{B5-1}} = \frac{n_{\mathrm{p}}}{2\pi f_1}I_{25}E_2\left[\cos(4\omega t-\phi_2+\frac{4\pi}{3})-\cos(6\omega t-\phi_2)\right] \tag{9}$$

$$T_{\mathrm{C5-1}} = \frac{n_{\mathrm{p}}}{2\pi f_1}I_{25}E_2\left[\cos(4\omega t-\phi_2+\frac{2\pi}{3})-\cos(6\omega t-\phi_2)\right] \tag{10}$$

The 5-vibration harmonic torque could be obtained by adding formula (8), (9), and (10)

$$T_{5-1} = \frac{3n_{\mathrm{p}}}{2\pi f_1}I_{25}E_2\cos(6\omega t-\phi_2) = \frac{3n_{\mathrm{p}}}{2\pi f_1}I_{25}E_2\cos(6\omega t+\pi-\phi_2) \tag{11}$$

From formula (11), it could be found that 6-times of the fundamental frequency rotor current in the rotor could be induced by 5th stator harmonic current, which interacted with the fundamental rotating magnetic field to form vibration torque [23]. The frequency of vibration torque was 6-times of the fundamental frequency of the rotor. Similarly, more vibration harmonic torques could be derived based on arbitrary stator harmonic current and arbitrary time harmonic magnetic field. And their vibration frequencies could be calculated based on the difference of harmonic number for stator harmonic current and time harmonic magnetic field.

2.2 Control strategy for traction motor

The structure diagram of the three-phase voltage inverter is illustrated in Fig. 1b. For the working principle, phase *U* as an reference, if the IGBT V_1 turned on, IGBT V_4 turned off, it was recorded as 1, and otherwise, it was recorded as 0. The working principle of each phase was the same, and there were eight states after three-phase combination, which were represented by $\boldsymbol{U}_0$~$\boldsymbol{U}_7$ respectively.

In direct torque control, there are two types of flux linkage control methods, i.e., hexagon flux linkage and circular flux linkage.

The circular flux linkage control method had the characteristics of large calculation, more switching times and small torque ripple, and it was suitable for low speed operation. The difference could be obtained by comparing between the measured value and the given value for rotor angular velocity, which would be used to obtain the reference value of electromagnetic torque by PI regulator. The reference value of flux was given directly by constant. The estimated values of torque and flux were compared with their reference values, respectively. The request signal of flux and torque were obtained by hysteresis comparator, as shown in Table 1 and Table 2.

Table 1. Control rules for circular track flux linkage.

Flux linkage deviation	ψQ value	Output voltage vector properties
$\psi_s^* - \lvert\psi_s\rvert \le -\varepsilon_\psi$	2	Voltage vector that reduce the flux linkage absolute value
$\lvert\psi_s^* - \lvert\psi_s\rvert\rvert \le \varepsilon_\psi$	Remain unchanged	Maintaining the original state of control
$\psi_s^* - \lvert\psi_s\rvert \ge \varepsilon_\psi$	1	Voltage vector that increase the flux linkage absolute value

Table 2. Torque control rules for circular trajectory.

Torque deviation	TQ value	Output voltage vector properties
$T_e^* - T_e \le -\varepsilon_T$	3	A vector that rotates the stator flux linkage back.
$T_e^* = T_e$	2	Output zero vector
$\lvert T_e^* - T_e\rvert < \varepsilon_T$	Remain unchanged	Maintaining the original state of control
$T_e^* - T_e \ge \varepsilon_T$	1	A vector that rotates the stator flux linkage forward

Then the information for looking up the table was obtained according to the request signal and the current stator flux vector space position. The corresponding switch signal could be found by directly searching the voltage vector, as shown in Table 3. Finally, the three-phase controllable AC could be achieved by inputting the switch signal into the inverter, and the torque of the traction motor could be controlled.

Table 3. Space voltage vectors with counter clockwise rotation.

ΨQ	TQ	θ(1)	θ(2)	θ(3)	θ(4)	θ(5)	θ(6)	θ(7)	θ(8)	θ(9)	θ(10)	θ(11)	θ(12)
1	1	$\boldsymbol{U}_2$	$\boldsymbol{U}_2$	$\boldsymbol{U}_3$	$\boldsymbol{U}_3$	$\boldsymbol{U}_4$	$\boldsymbol{U}_4$	$\boldsymbol{U}_5$	$\boldsymbol{U}_5$	$\boldsymbol{U}_6$	$\boldsymbol{U}_6$	$\boldsymbol{U}_1$	$\boldsymbol{U}_1$
	2	$\boldsymbol{U}_0$	$\boldsymbol{U}_7$	$\boldsymbol{U}_0$	$\boldsymbol{U}_7$	$\boldsymbol{U}_0$	$\boldsymbol{U}_7$	$\boldsymbol{U}_0$	$\boldsymbol{U}_7$	$\boldsymbol{U}_0$	$\boldsymbol{U}_7$	$\boldsymbol{U}_0$	$\boldsymbol{U}_7$
	3	$\boldsymbol{U}_6$	$\boldsymbol{U}_1$	$\boldsymbol{U}_1$	$\boldsymbol{U}_2$	$\boldsymbol{U}_2$	$\boldsymbol{U}_3$	$\boldsymbol{U}_3$	$\boldsymbol{U}_4$	$\boldsymbol{U}_4$	$\boldsymbol{U}_5$	$\boldsymbol{U}_5$	$\boldsymbol{U}_6$
2	1	$\boldsymbol{U}_3$	$\boldsymbol{U}_4$	$\boldsymbol{U}_4$	$\boldsymbol{U}_5$	$\boldsymbol{U}_5$	$\boldsymbol{U}_6$	$\boldsymbol{U}_6$	$\boldsymbol{U}_1$	$\boldsymbol{U}_1$	$\boldsymbol{U}_2$	$\boldsymbol{U}_2$	$\boldsymbol{U}_3$
	2	$\boldsymbol{U}_7$	$\boldsymbol{U}_0$	$\boldsymbol{U}_7$	$\boldsymbol{U}_0$	$\boldsymbol{U}_7$	$\boldsymbol{U}_0$	$\boldsymbol{U}_7$	$\boldsymbol{U}_0$	$\boldsymbol{U}_7$	$\boldsymbol{U}_0$	$\boldsymbol{U}_7$	$\boldsymbol{U}_0$
	3	$\boldsymbol{U}_5$	$\boldsymbol{U}_5$	$\boldsymbol{U}_6$	$\boldsymbol{U}_6$	$\boldsymbol{U}_1$	$\boldsymbol{U}_1$	$\boldsymbol{U}_2$	$\boldsymbol{U}_2$	$\boldsymbol{U}_3$	$\boldsymbol{U}_3$	$\boldsymbol{U}_4$	$\boldsymbol{U}_4$

The hexagon flux linkage method had the characteristics of less switching times, simple control circuit logic and easy implementation. Stator voltage and current could be used to obtain the flux in two-phase static coordinate system. Then that flux was compared with the given flux to obtain corresponding switching value. The adjustment of torque was used to determine whether to insert zero voltage vector. Correct voltage state signal was selected to generate the desired hexagon flux linkage.

Hexagon flux trajectory was adopted for flux weakening control method in this study, which was used in the speed control of traction motor above the rated speed. By reducing the given value of stator flux, the speed of flux was accelerated, the torque could increase, and then the speed in turn would increase. The flux weakening control adopts full voltage operation mode, and no zero voltage vector was added to adjust the given value of stator flux dynamically.

2.3 Vehicle system dynamics model

In order to analyse the torsion vibration characteristics of the transmission system, the vehicle transmission system was simplified as follows: (1) The movement gap of each component in the transmission system was ignored, (2) The effect of friction between components was not considered, (3) The quality of each component in the transmission system was set as a centralized quality point.

The rail vehicle system, as shown in Fig. 2, consisted of 4 wheel sets [40] [41], 8 axle boxes, 4 gear boxes, 4 pairs of gears, 4 motors, 4 motor rotors, 2 frames and 1 car-body. When building the model, the stator and the body of the traction motor were considered as a whole, and which connected with the frame through three rubber nodes [42], the motor rotor was an individual, rotating relative to the motor stator. The big gear and small gear within the gearbox had an independent freedom degree, the small gear and its shaft were considered as a whole, and the big gear was consolidated with the axle through constraints.

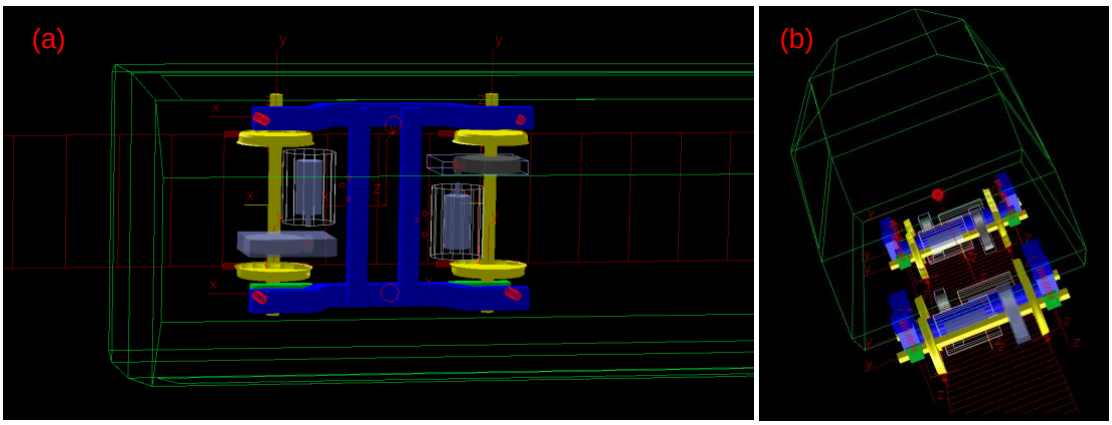

Figure 2. Top view (a) and plan view (b) of the vehicle dynamics model with transmission system.

3 Results and discussion

Using the electro-mechanical coupling multi-body dynamic vehicle model, the analysis of typical operating conditions was performed. By comparing with the line test, the influence of the traction system on the motor and gearbox was studied.

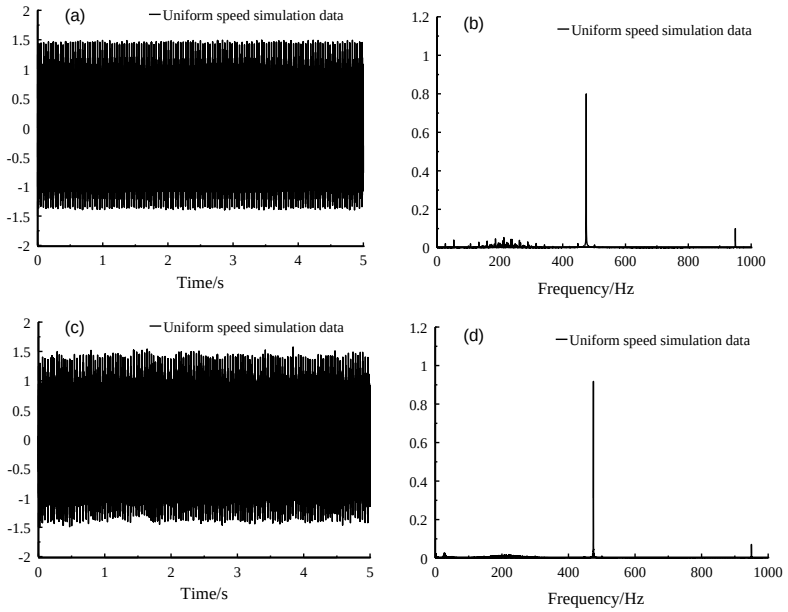

Figure 3. Motor longitudinal vibration acceleration, (a-b) orbit free spectrum, (c-d) orbital spectrum.

A remarkable frequency peak at 473Hz exhibited in frequency domain diagram for motor longitudinal vibration under uniform speed condition, shown in Fig. 3, which is 12-times of the fundamental frequency of the motor rotor. It was caused by the vibration harmonic torque, which was generated by the interaction between the 11th and 13th harmonic currents and the fundamental flux. Meanwhile, the vibration amplitude was below 1.5 m/s^2 with or without orbital spectrum in time domain diagram of motor longitudinal vibration.

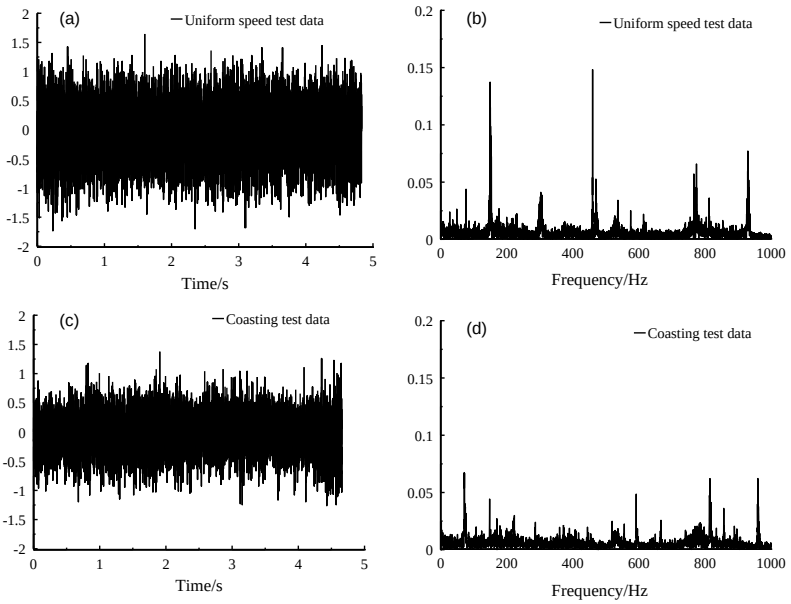

Figure 4. Motor longitudinal vibration acceleration, at (a-b) uniform speed, (c-d) coasting condition.

From the frequency domain diagram in Fig. 4, the vibration amplitudes at 154Hz and 469Hz were significant under the uniform speed condition (Fig. 4b). While under the coasting condition in Fig. 4d, the frequency 469Hz disappeared, and the amplitude of frequency 154Hz was much lower than

at uniform speed. The vibration amplitude at uniform speed condition was a little larger than that at coasting condition in time domain diagram for motor longitudinal vibration.

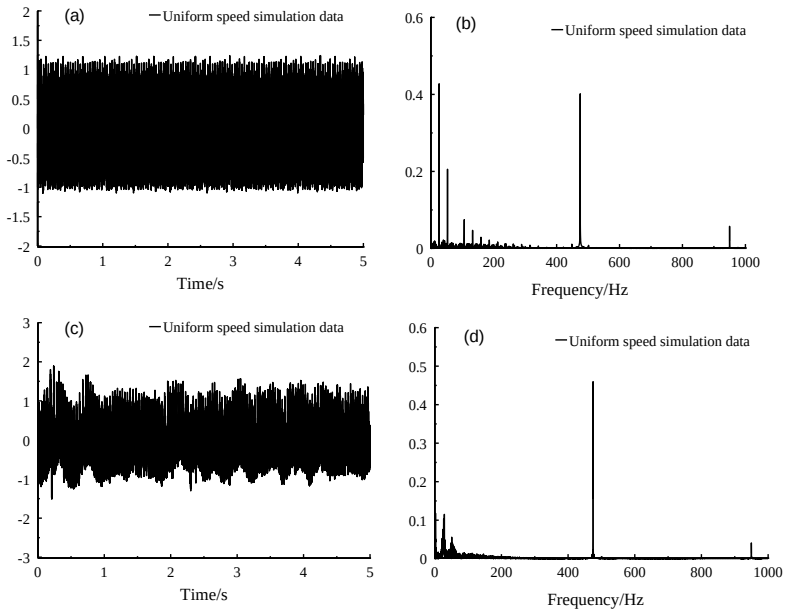

Figure 5. Gearbox longitudinal vibration acceleration, (a-b) orbit free spectrum, (c-d) orbital spectrum.

For the influence of orbital load spectrum, the gearbox longitudinal vibration acceleration under uniform speed were compared and shown in Fig. 5. The vibration acceleration of gearbox without orbital spectrum (Fig. 5a) was a little lower than that of gearbox with orbital spectrum. A remarkable frequency peak at 473Hz could still be observed at both conditions, and frequency distribution changed slightly by the introduce of orbital spectrum.

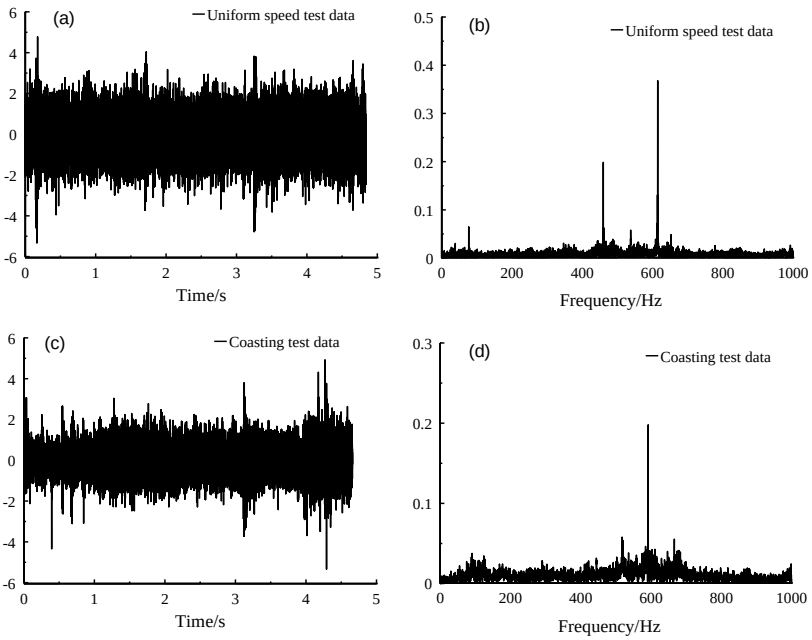

Figure 6. Gearbox longitudinal vibration acceleration, at (a-b) uniform speed, (c-d) coasting condition.

At the uniform speed condition in Fig. 6b, two significant frequency peaks could be found, i.e., 469Hz and 628Hz. While the frequency peak at 469Hz nearly could not be identified in the case of coasting condition (Fig. 6d). As for the vibration acceleration, the amplitude at coasting condition was slightly smaller than that at uniform speed. These indicated that the influence of 12-times fundamental frequency (469Hz) of the rotor on the longitudinal direction of the gearbox disappeared quickly after the power supply was cut off.

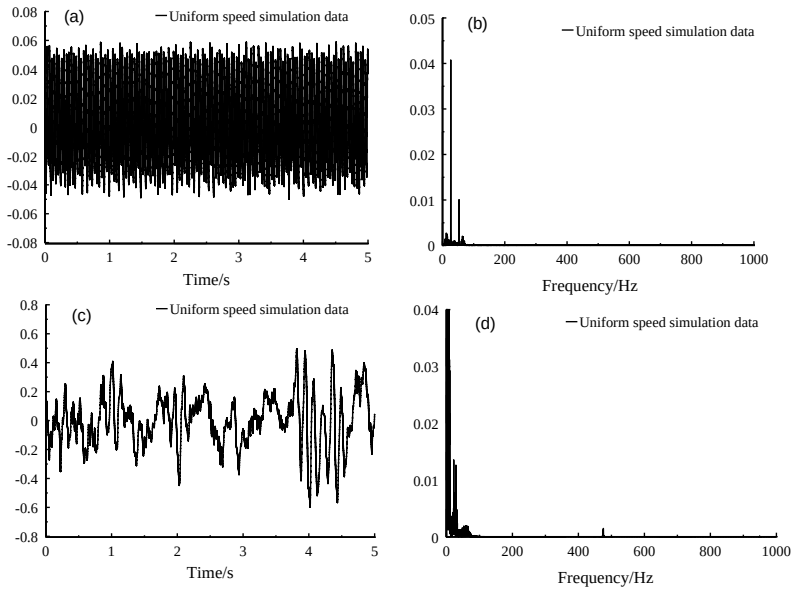

Figure 7. Motor lateral vibration acceleration, (a-b) orbit free spectrum, (c-d) orbital spectrum.

In the spectrum diagram of Fig. 7 for motor lateral vibration acceleration, it can be found that the frequency was mainly below 100Hz, and vibration acceleration was most intense at 20-40Hz especially at the condition of orbital spectrum. The vibration amplitude with orbital spectrum (Fig. 7c) was far greater than that without orbital spectrum, by one order.

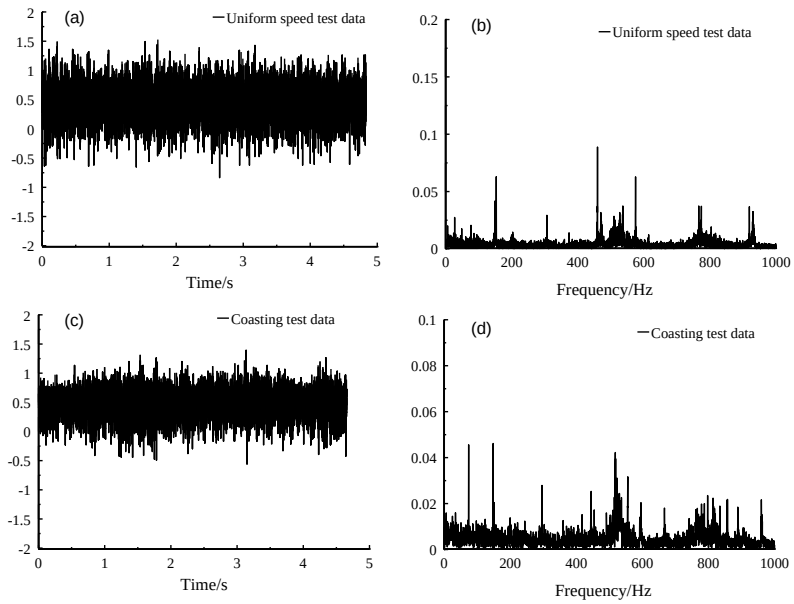

Figure 8. Motor lateral vibration acceleration, at (a-b) uniform speed, (c-d) coasting condition.

In frequency domain diagram of Fig. 8 for motor lateral vibration acceleration, vibration frequency peak at 469Hz was identified under two conditions, i.e., uniform speed and coasting, and its amplitude was 0.09 m/s^2 at uniform speed and 0.028 m/s^2 at coasting condition. In time domain diagram, vibration amplitude at uniform speed (Fig. 8a) was a slightly larger than that at coasting condition.

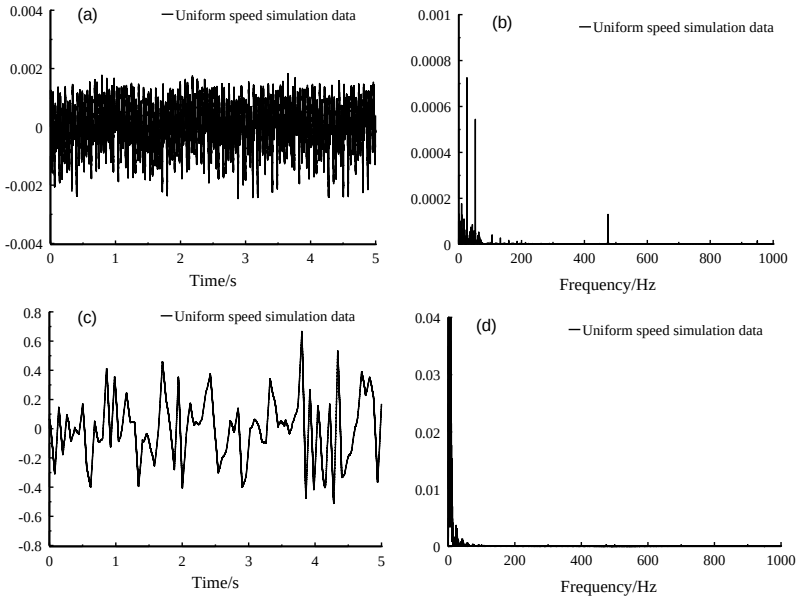

Figure 9. Gearbox lateral vibration acceleration, (a-b) orbit free spectrum, (c-d) orbital spectrum.

In frequency domain diagram for gearbox lateral vibration without orbital spectrum (Fig. 9b), vibration frequency was mainly distributed in 0-70Hz, but also a 12-times of the fundamental frequency of the rotor can be identified in high frequency at ~470Hz. When orbital spectrum was introduced (Fig. 9d), low frequency vibration became dominating (Fig. 9d), high frequency peak nearly disappeared.

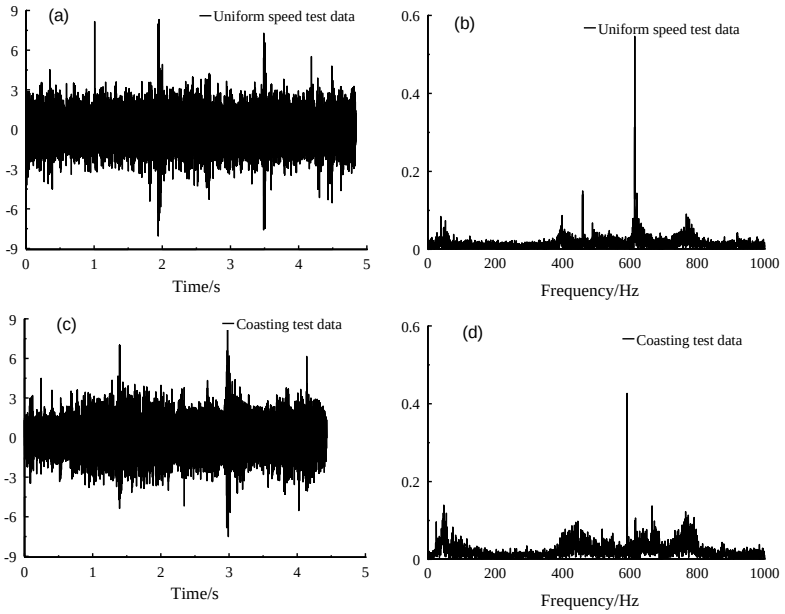

Figure 10. Gearbox lateral vibration acceleration, at (a-b) uniform speed, (c-d) coasting condition.

In frequency domain diagram for gearbox lateral vibration (Fig. 10), the meshing frequency, i.e., 628Hz, was prominent at both the two conditions. At uniform speed in Fig. 10b, a vibration peak at 469Hz could also be found, which was 12 times of the fundamental frequency of the rotor, while it nearly disappeared at coasting condition.

4 Conclusions

With the increase of the speed of rail vehicles, the dynamic performance of the train system becomes more and more complex, especially the transmission system, which is the main power source and the main transmission component of traction. In this work, a vehicle electro-mechanical coupling mathematical model based on multi-body dynamics was established by explicitly incorporating the electric-induced traction into the transmission system, to study the influence of traction system vibration on vehicle dynamics. The natural vibration characteristics of the traction drive system were analyzed, by comparison with field test, it was observed that there was a vibration peak of 12-times of the fundamental rotor frequency on the motor and gearbox, which exists at uniform speed. And a vibration peak of meshing frequency on the gearbox exists at conditions of uniform speed and coasting.

Acknowledgments

The financial support of Science and Technology Project of Chongqing Education Commission (KJ1505702), and Construction Project of Chongqing High Level Vocational Schools and Specialty Groups (Chongqing Vocational College of Transportation) are gratefully acknowledged.

References

[1] Zhang, T., Li, D., & Qiao, Y. (2018). Comprehensive optimization of urban rail transit timetable by minimizing total travel times under time-dependent passenger demand and congested conditions. *Applied Mathematical Modelling, 58*, 421-446.

[2] Zeng, Z.-p., et al. (2020). Wheel-rail stochastic dynamics and rail wear analysis of small radius curved sections of a tram line based on generalized probability density evolution. *Proceedings of the Institution of Mechanical Engineers Part F-Journal of Rail and Rapid Transit.*

[3] Ma, H., et al. (2020). Influence of Full-Life Cycle Wheel Profile on the Contact Performance of Wheel and Standard Fixed Frog in Heavy Haul Railway. *Shock and Vibration, 2020.*

[4] Ma, C., et al. (2021). The initiation mechanism and distribution rule of wheel high-order polygonal wear on high-speed railway. *Engineering Failure Analysis, 119.*

[5] Zhang, G., et al. (2019). Inverter Operating Characteristics Optimization for DC Traction Power Supply Systems. *IEEE Transactions on Vehicular Technology, 68(4)*, 3400-3410.

[6] Huang, X., et al. (2021). A TOD Planning Model Integrating Transport and Land Use in Urban Rail Transit Station Areas. *IEEE Access, 9*, 1103-1115.

[7] Yuan, Z., Tian, C., & Wu, M. (2020). Modelling and parameter identification of friction coefficient for brake pair on urban rail vehicle. *International Journal of Rail Transportation.*

[8] Wang, H., et al. (2020). A Bayesian Network Approach for Condition Monitoring of High-Speed Railway Catenaries. *IEEE Transactions on Intelligent Transportation Systems, 21(10)*, 4037-4051.

[9] Lei, Y., et al. (2018). An Improved Torque and Current Pulsation Suppression Method for Railway Traction Drives Under Fluctuating DC-Link Voltage. *IEEE Transactions on Power Electronics, 33(10)*, 8565-8577.

[10] Liu, Q., Liang, T., & Dinavahi, V. (2020). Real-Time Hierarchical Neural Network Based Fault Detection and Isolation for High-Speed Railway System Under Hybrid AC/DC Grid. *IEEE Transactions on Power Delivery, 35(6)*, 2853-2864.

[11] Hao, F., et al. (2020). Optimal Voltage Regulation and Power Sharing in Traction Power Systems With Reversible Converters. *IEEE Transactions on Power Systems, 35(4)*, 2726-2735.

[12] Liu, B., et al. (2020). Analysis and Optimization of Driving Attitude and Oscillation Characteristics of Suspension-Type Small Rail Vehicles. *Shock and Vibration, 2020.*

[13] Zhang, H., et al. (2020). Properties of Chinese railway network: Multilayer structures based on timetable data. *Physica a-Statistical Mechanics and Its Applications, 560.*

[14] Li, R., et al. (2020). Segmented Power Supply Preset Control Method of High-Speed Rail Contactless Traction Power Supply System considering Regenerative Braking Energy Recovery. *Mathematical Problems in Engineering, 2020.*

[15] Chen, J., et al. (2019). The Harmonic Characteristic of the Advanced Synchronous SVPWM Overmodulation Strategy. *IEEE Access, 7*, 148934-148949.

[16] Luo, R., et al. (2020). A nonlinear rubber spring model for the dynamics simulation of a high-speed train. *Vehicle System Dynamics, 58*(9), 1367-1384.

[17] Guo, J., et al. (2020). Field Measurements of Vibration on the Car Body-Suspended Equipment for High-Speed Rail Vehicles. *Shock and Vibration, 2020*, 6041543.

[18] Bao, K., et al. (2021). Fatigue life of the welding seam of a tracked vehicle body structure evaluated using the structural stress method. *Engineering Failure Analysis, 120*.

[19] Li, F., et al. (2019). Vibration fatigue dynamic stress simulation under multi-load input condition: Application to metro lifeguard. *Engineering Failure Analysis, 99*, 141-152.

[20] Li, F.S., H. Wu, & P.B. Wu. (2021). Vibration fatigue dynamic stress simulation under non-stationary state. *Mechanical Systems and Signal Processing, 146*.

[21] Wang, Q., et al. (2018). Carbody vibrations of high-speed train caused by dynamic unbalance of underframe suspended equipment. *Advances in Mechanical Engineering, 10*(12), 1-13.

[22] Lu, Z., et al. (2021). Coupling model and vibration simulations of railway vehicles and running gear bearings with multitype defects. *Mechanism and Machine Theory, 157*.

[23] Xu, K., J. Zeng, & L. Wei. (2019). An analysis of the self-excited torsional vibration of high-speed train drive system. *Journal of Mechanical Science and Technology, 33*(3), 1149-1158.

[24] Lei, Z., & Z. Wang. (2020). Contact and creep characteristics of wheel-rail system under harmonic corrugation excitation. *Journal of Vibration and Control*.

[25] Gong, D., J.S. Zhou, & W.J. Sun. (2016). Influence of under-chassis-suspended equipment on high-speed EMU trains and the design of suspension parameters. *Proceedings of the Institution of Mechanical Engineers Part F-Journal of Rail and Rapid Transit, 230*(8), 1790-1802.

[26] Liu, J., & S. Du. (2020). Dynamic Analysis of a High-Speed Railway Train With the Defective Axle Bearing. *International Journal of Acoustics and Vibration, 25*(4), 525-531.

[27] Huang, C., & J. Zeng. (2018). Dynamic behaviour of a high-speed train hydraulic yaw damper. *Vehicle System Dynamics, 56*(12), 1922-1944.

[28] Wu, Q., et al. (2020). Curving resistance from wheel-rail interface. *Vehicle System Dynamics*.

[29] Zhang, S., et al. (2020). Dynamic wheel-rail interaction at high speed based on time-domain moving Green's functions. *Journal of Sound and Vibration, 488*.

[30] Wang, B., et al. (2020). An investigation into the fatigue failure of metro vehicle bogie frame. *Engineering Failure Analysis, 118*.

[31] Deng, X., et al. (2019). European high-speed bogie technology review. *International Journal of Vehicle Design*, *79*(1), 43-62.

[32] Wang, J., et al. (2020). Nonsmooth Dynamics of a Gear-Wheelset System of Railway Vehicles Under Traction/Braking Conditions. *Journal of Computational and Nonlinear Dynamics*, *15*(8).

[33] Xu, K., et al. (2020). Optimal profile design for rail grinding based on wheel-rail contact, stability, and wear development in high-speed electric multiple units. *Proceedings of the Institution of Mechanical Engineers Part F-Journal of Rail and Rapid Transit*, *234*(6), 666-677.

[34] Li, M., et al. (2021). Dynamic response analysis of train-induced vibration impact on the Probhutaratna pagoda in Beijing. *Earthquake Engineering and Engineering Vibration*, *20*(1), 223-243.

[35] Lei, S., Y. Ge, & Q. Li. (2020). Effect and its mechanism of spatial coherence of track irregularity on dynamic responses of railway vehicles. *Mechanical Systems and Signal Processing*, *145*.

[36] Liao, B., & Y. Luo. (2020). Influence of alignments of guide curves on the passing performance of railway turnout diverging route. *Vehicle System Dynamics*.

[37] Cui, L. (2014). *Vibration Characteristic Analysis of Driving System for High-Speed Trains*. Southwest Jiaotong University.

[38] Fan, T., Z. Ren, & R. Xue. (2021). Load variation of the wheel-mounted brake disc bolts of a high-speed train. *Engineering Failure Analysis*, *119*.

[39] Xu, L., et al. (2020). Modelling of vehicle-track related dynamics: a development of multi-finite-element coupling method and multi-time-step solution method. *Vehicle System Dynamics*.

[40] Ye, Y., & Y. Sun. (2020). Reducing wheel wear from the perspective of rail track layout optimization. *Proceedings of the Institution of Mechanical Engineers Part K-Journal of Multi-Body Dynamics*.

[41] Zhang, W., et al. (2020). Research on the Simulation of Wheelset Response Characteristic Identification of Railway Fastener Loosening. *Mathematical Problems in Engineering*, *2020*.

[42] Xiao, H., et al. (2020). Analysis on mechanical characteristics of welded joint with a new reinforced device in high-speed railway. *Advances in Mechanical* Engineering, *12*(10).